

SOLAR PASSIVE DISTILLER WITH HIGH PRODUCTIVITY AND MARANGONI EFFECT-DRIVEN SALT REJECTION - SUPPLEMENTARY INFORMATION

Matteo Morciano^{a,b,c}, Matteo Fasano^{a,b}, Svetlana V. Boriskina^c, Eliodoro Chiavazzo^a, and Pietro Asinari^{a,d}

^a*Department of Energy, Politecnico di Torino, Corso Duca degli Abruzzi 24, 10129 Torino, Italy*

^b*Clean Water Center, Politecnico di Torino, Corso Duca degli Abruzzi 24, 10129 Torino, Italy*

^c*Department of Mechanical Engineering, Massachusetts Institute of Technology, Cambridge, Massachusetts 02139, USA*

^d*INRIM Istituto Nazionale di Ricerca Metrologica, Strada delle Cacce 91, Torino 10135, Italy.*

1 Supplementary Note: Components of the prototype

The main components of the distiller are summarized in Supplementary Fig. S1.

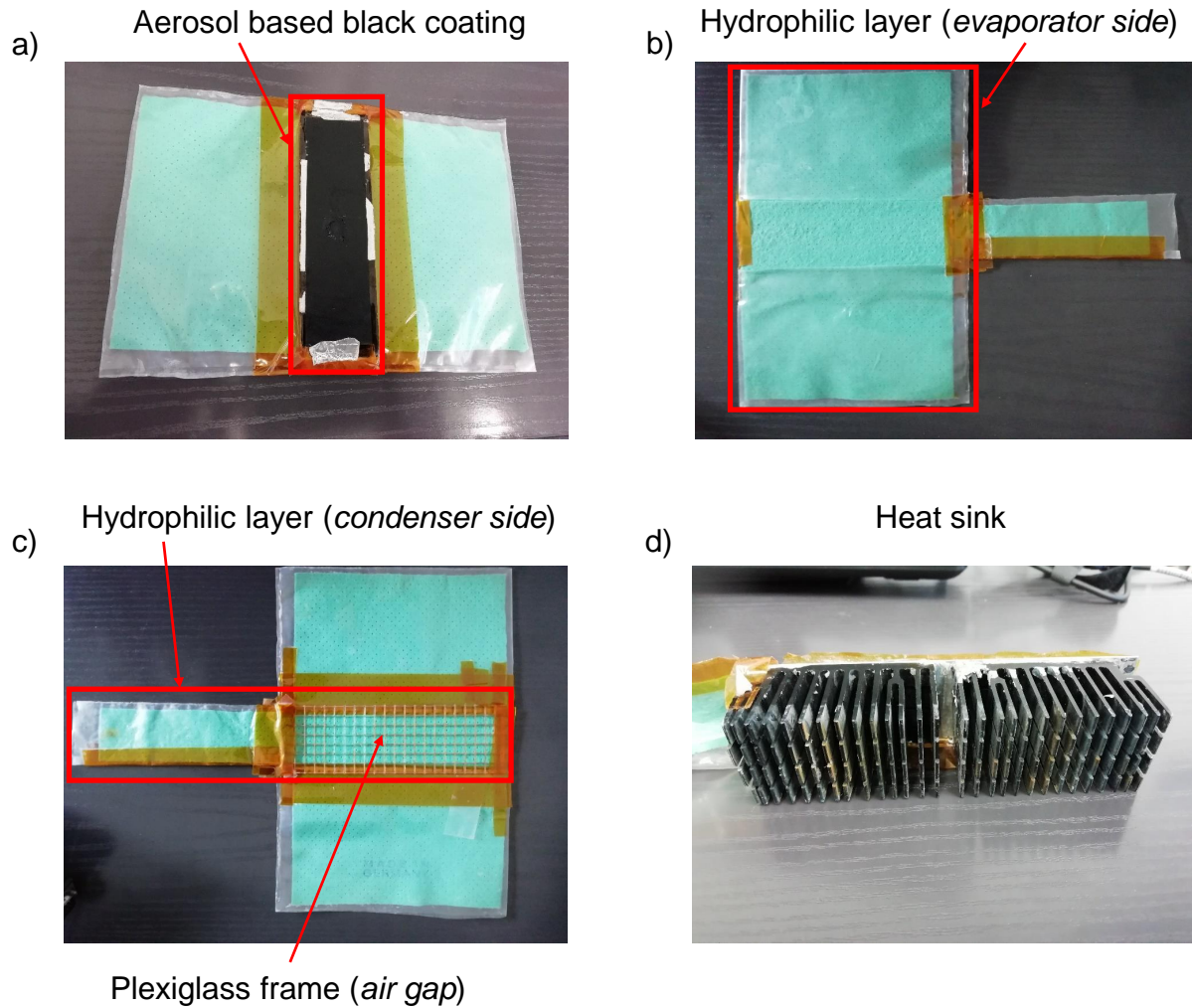


Figure S 1. Main components of the solar desalination prototype. a) Aerosol based black absorber (Zynolyte[®] Hi-Temp aerosol spray paint); b) hydrophilic layer (evaporator side); c) hydrophilic layer (condenser side) and plexiglass frame (porous air gap); d) heat sink for rejecting the heat in the saltwater basin. Note that input and output strips are not directly exposed to air during experiments: each strip is covered by a LLDPE film to suppress natural evaporation towards the surrounding ambient.

2 Supplementary Note: Description of the prototype

The proposed device represents a synergy between the passive and multi-stage device with enhanced yield reported in ref. [1] and the salt rejecting solution described in ref. [2]. Here, the approaches are rationalized for both enhancing distillate productivity and salt rejection in passive solar desalination systems.

In Supplementary Fig. S2, the resizing procedure, of the evaporating and salt rejecting areas is summarized, and the evaporator and condenser surfaces are schematically shown for both devices.

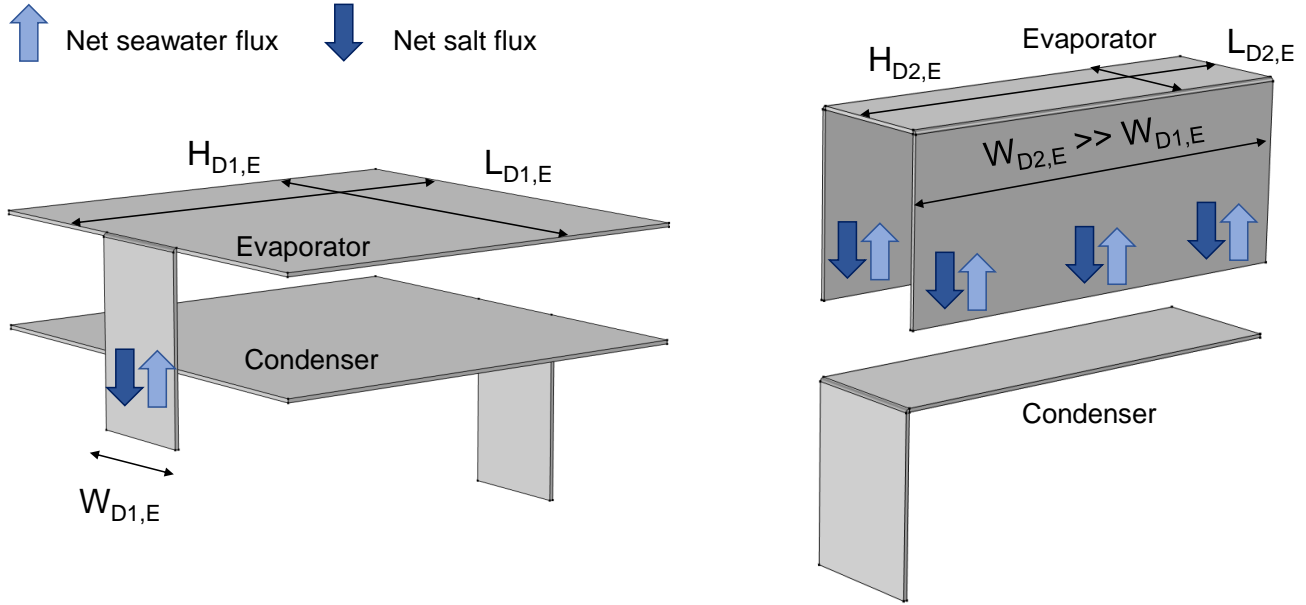


Figure S 2. Illustrative picture of the geometry of the distillers: details on the salt rejecting and evaporating areas for the device reported in ref. [1] and the current version. The size of the evaporator and condenser in case of ref. [1] and current distiller are shown on the left and on the right side, respectively.

First, in the current device (on the right in Supplementary Fig. S2), the width of the strips/channels through which seawater is supplied by capillary action to each evaporator is increased (namely $W_{D2,E} = 12 \text{ cm} > W_{D1,E} = 3 \text{ cm}$). In addition, the seawater reaches each evaporator via both sides rather than one, thus increasing the salt rejecting surfaces and, as consequence, improving the rejection performance (see blue arrows). Finally the horizontal extension of the hydrophilic layers is reduced (namely $L_{D2,E} = 3.5 \text{ cm} < L_{D1,E} = 12 \text{ cm}$). Therefore, the longest path that the salt particles have to cover to reach the border and to flow back to the sea is minimized and reduced by a factor ≈ 7 ($\approx \frac{L_{D1,E}}{L_{D2,E}}$).

Moreover, in the current distiller the selective absorber used in ref. [1] is substituted by a more robust aerosol-based black paint, and the 3D printed convection reducer is removed. Removing the convection reducer is a good strategy for improving the long-term stability, since these films suffer from ultraviolet degradation (yellowing and clouding) limiting the useful life of the product. In addition, the membrane (thermal conductivity equal to $472 \text{ W m}^{-2} \text{ K}^{-1}$) is substituted with a plexiglass spacer (thermal conductivity equal to $42 \text{ W m}^{-2} \text{ K}^{-1}$, which means $\approx 91\%$ reduction compared to the classic membrane-based solution) that creates the air gap between the evaporator and the condenser. In table S1, the main differences between the solar passive multistage device reported in ref. [1] and the here developed distiller are summarized.

Further details on the air gap and solar absorber are reported in the Supplementary Notes 3.2 and 3.4.

	Ref. [1]	Current Distiller
Evaporating area	$A_{D1} = L_{D1,E} \times H_{D1,E}$	$A_{D2} \approx 0.3 L_{D1,E} \times H_{D1,E}$
Salt-rejecting length	$W_{D1,E}$	$2W_{D2,E} = 8 \times W_{D1,E}$
Gap	Membrane ($d_m \approx 150 \mu\text{m}$)	Spacer ($d_a \approx 1.65 \text{ mm}$)
Solar absorber	Selective - TiNOX [®]	Black paint - Zynolyte [®]

Table S 1. Main differences between the solar passive multistage device reported in ref. [1] and the here developed distiller. Note that $L_{D1,E} = H_{D1,E} = H_{D2,E} = W_{D2,E} = 12 \text{ cm}$ and $W_{D1,E} \approx 3 \text{ cm}$. Details on evaporating area and salt-rejecting length are reported in Supplementary Fig. S2, whilst details on the used gap between evaporator and condenser and the solar absorber are discussed in Supplementary Notes 3.2 and 3.4.

3 Supplementary Note: Characterization of the components of the prototype

3.1 Wicking properties of hydrophilic layer

An experimental campaign is carried out to characterize the wicking properties of the hydrophilic layer employed as evaporator/condenser. In detail, the hydrophilic layer should be able to drive water from the sea level to each evaporator of the modular device exploiting only capillary action. Then, a suitable and sufficient capillary rise (namely h , measured in m) has to be ensured. In addition, the ability of the porous material to allow fluids to pass through has to be as large as possible. This second key parameter is the permeability (namely k , measured in m^2) which depends on the porosity ($\epsilon = \frac{V_{VOID}}{V_{SAMPLE}}$, namely the ratio between the volume of air and sample).

Capillary rise. In Supplementary Fig. S3, the experimental setup used for measuring the capillary rise is shown. The hydrophilic layer is immersed in a colored distilled water basin and the final level, reached by the water, is measured. Different materials suitable for the hydrophilic layer of the distiller have been tested.

The first option is to use the cellulose-based fabric (commercially known as Zorb) exploited in the floating solar still described in ref. [2] (see white sample in Supplementary Fig. S3). However, this wick is not a suitable option to be used in a modular device, since the limited capillary rise (≈ 3.5 cm) is not sufficient for feeding each evaporator. Thus, dry out is observed in the stage farthest from the free surface of the 3-stage configuration device. A commercial viscous fiber-based wick (commercially known as Sungbocleamy), see sample on the right in Supplementary Fig. S3A, is then tested, proving a sufficient capillary rise (≈ 5.5 cm).

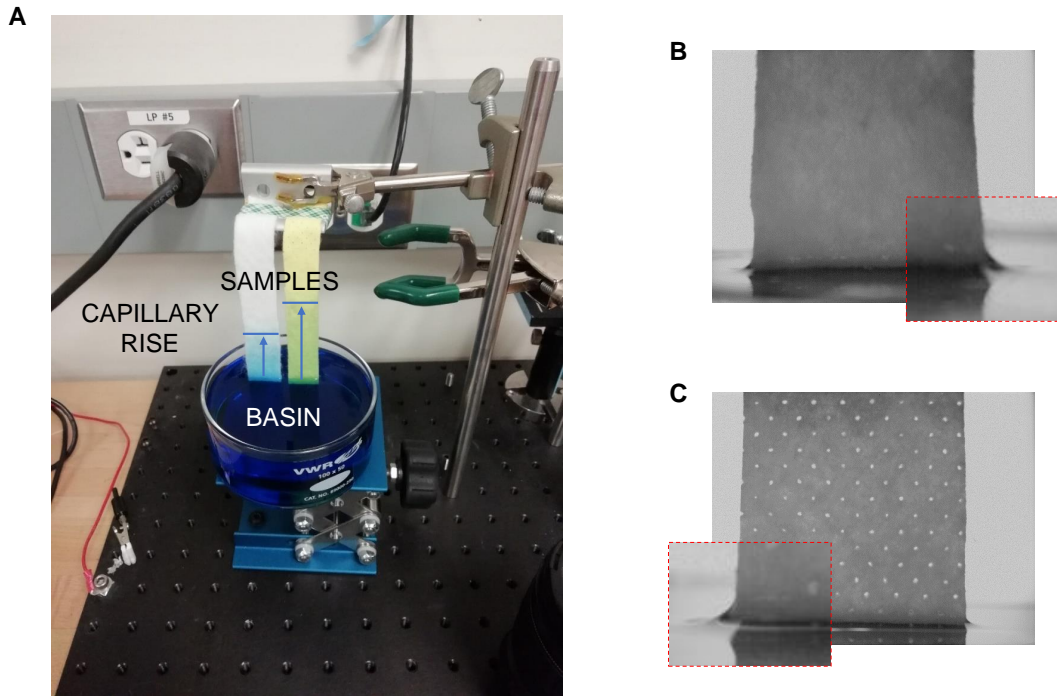


Figure S 3. A) Experimental setup for measuring the capillary rise; B) contact angle measurements of the Zorb hydrophilic layer; C) contact angle measurements of the Sungbocleamy hydrophilic layer.

It is worth to point out that the capillary rise of water in a sample, namely h , mainly depends on the pore size and contact angle. [3] In detail, the driving capillary pressure is defined as:

$$\Delta P_{cap} = \rho gh = \frac{2\gamma_g \cos(\theta)}{r} \quad (1)$$

where γ_{lg} is the surface tension at the liquid gas interface, θ is the contact angle and r is the average pore size. The contact angle is measured with an imaging analysis software and it is equal to $\approx 27.5^\circ$ (see Figs. S3B and C).

Porosity. Then, the porosity of the hydrophilic layers (Sungbocleamy) is evaluated. In detail, a wick sample is immersed in a ticked basin filled with deionized water. The volume variation, measured through the height of the liquid column, corresponds to the volume occupied by the fibers of the hydrophilic layer itself. The evaluated porosity is equal to 0.900 ± 0.033 .

Permeability. Another key parameter that has to be considered is the permeability of the porous medium, which is related to the porosity, but also to the shape of the pores in the medium and their level of connectedness. This property is evaluated by measuring the propagation of the fluid through the hydrophilic layer (Sungbocleamy) as function of time.

The experimental setup (see Supplementary Fig. S4) consists of: 1) a water basin filled with deionized water, 2) a initially dried wick sample, 3) a sample clip and 4) a high speed camera. Once one extremity is immersed in the water basin, the water starts to rise through sample and the wicking process monitored by the high speed camera (Vision research Phantom 7.1). An imaging analysis software is used for post processing the frames.

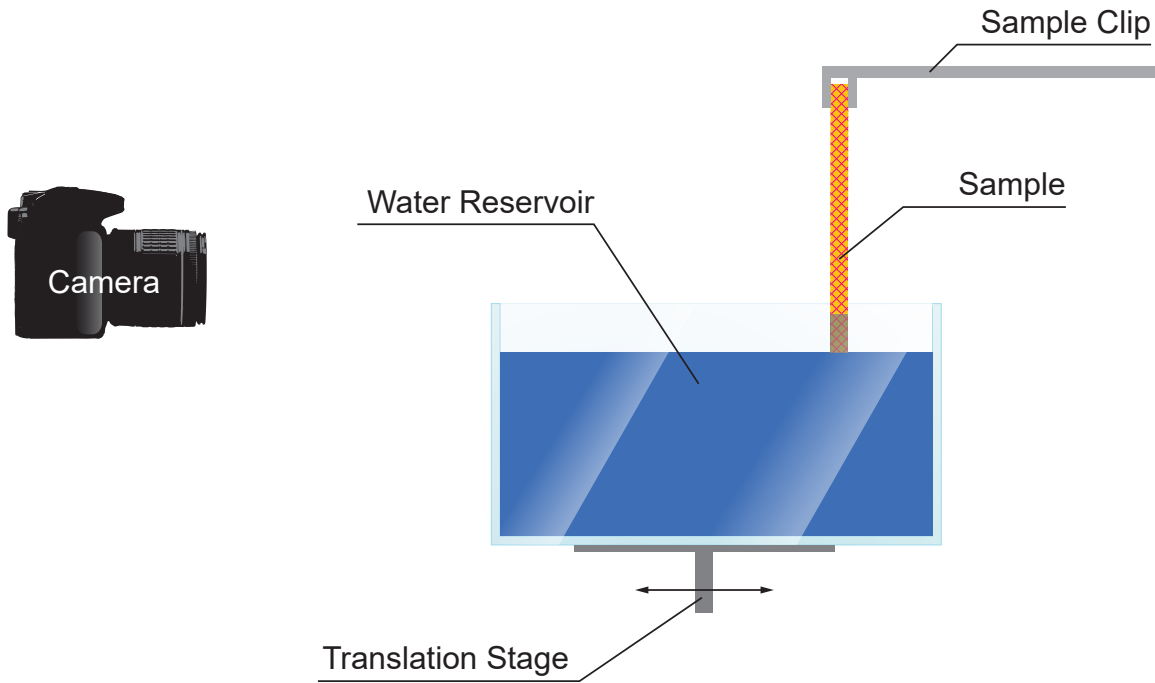


Figure S 4. Experimental setup for measuring the permeability of the hydrophilic layer.

In Supplementary Fig. S5, red circles and blue squares represent data of two different experiments carried out for proving the repeatability of the measurements. The inset is a zoom-in of the most populated zone of data. These data, namely the fluid propagation front as function of time, are fitted using the Darcy's equation with gravitational effect, and the permeability coefficient evaluated as [4]:

$$\frac{dy}{dt} = \frac{-k}{\mu\epsilon} \left(\frac{-\Delta P_{cap}}{y} - \rho g \right) \quad (2)$$

where y is the vertical coordinate and represents the position of the propagation front with time, k is the permeability of the wick (measured in m^2), μ and ρ are the viscosity and density of water, respectively. ΔP_{cap} is the driving capillary pressure, which acts against the gravity g (see eq. 1).

The permeability of the wick can be found explicitly by using the following relation [4], where k is the fitting parameter:

$$t = \frac{A \ln(A - By) + By - A \ln(A)}{B^2} \quad (3)$$

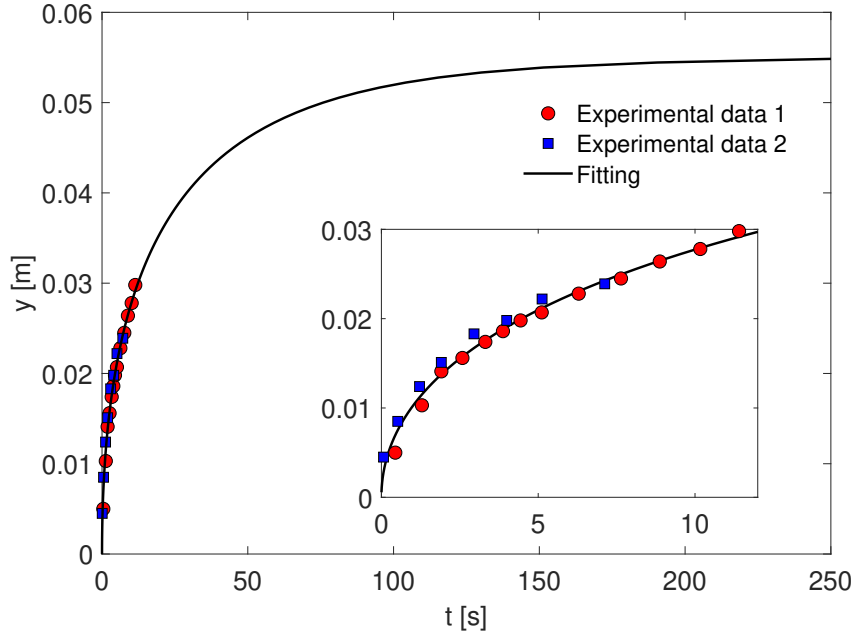


Figure S 5. Liquid front propagation as function of time, measured to estimate the permeability of the wick. Red circles and blue squares represent data of two independent experiments. Black line refers to equation 3.

$$A = \frac{k\Delta P_{cap}}{\mu\epsilon} \quad (4)$$

$$B = \frac{k\rho g}{\mu\epsilon} \quad (5)$$

The fitted permeability value on the experimental results reported in Supplementary Fig. S5 is equal to $\approx 1.0 \times 10^{-10} m^2$, with $R^2 = 0.99$. This value is important for understanding and studying possible advective components of the flow in a porous medium, which may affect the discharging process of the accumulated salt.

3.2 Mass transfer through air gap

Air gap optimization. In traditional membrane distillation (MD), the flow rates and temperature drop (order of magnitude $\approx 10^\circ\text{C}$ between evaporator and condenser) are actively controlled via pumps and thermostats, respectively. Thus, in traditional MD application, it has been demonstrated that hundred microns represents the optimal thickness for maximizing the distillate flow rate, aiming at keeping high permeability but low thermal conductivity at the same time. [5]

On the other hand, in case of passive and quasi-static conditions where temperatures are not imposed at the inlet channels of the device but are a consequence of the available solar flux and the thermal insulation given by the stratigraphy, an air gap of hundreds microns would be responsible of low distillate flow rates due to the almost negligible temperature drop (namely 1-2 order of magnitude smaller with respect to classic MD module). Hence, the theoretical model described in Supplementary Note 8 is used for optimizing sensitivity analysis figuring out the best air gap thickness and thus the maximum distillate productivity of the passive distiller.

Contrarily to the previous version of the distiller [1], where a commercial hydrophobic membrane was used for separating the evaporator from the condenser, here a tailored plastic porous frame is used (see Supplementary Fig. S6, left-hand side panel).

Two parameters of the spacer affect the vapour flux, namely the normalized effective area through which the vapour flows, indicated as γ_{spacer} , and the porosity ϵ_{spacer} . As far as concerns the normalized effective area, a calipers is used to measure $\gamma_{spacer} = 0.743 \pm 0.167$. The porosity, defined as ratio between volumes (namely $\epsilon_{spacer} = \frac{V_{VOID}}{V_{TOT}}$) is equal to $\epsilon_{spacer} = 0.805 \pm 0.065$, which has been evaluated using a scale with a precision of 0.001 g and considering the bulk density of plexiglass (1.18 g cm^{-3}). The mismatch between γ_{spacer} and ϵ_{spacer} values is due to the high operating temperature during the prototyping process, done by laser cutter. In fact, the plexiglass spacer presents areas where the material is slightly melted thus causing micro-metric variations in the average thickness of the spacer. However, these variations do not affect the distillate productivity neither in terms of mass flow rate nor in terms of salt contamination.

In Supplementary Fig. S6, the model predictions, in case of 1-stage configuration device, are shown. In the sensitivity analysis reported in Supplementary Fig. S6 (right-hand side) carried out with the model detailed in the Supplementary Note 8, the average values of γ_{spacer} and ϵ_{spacer} are used.

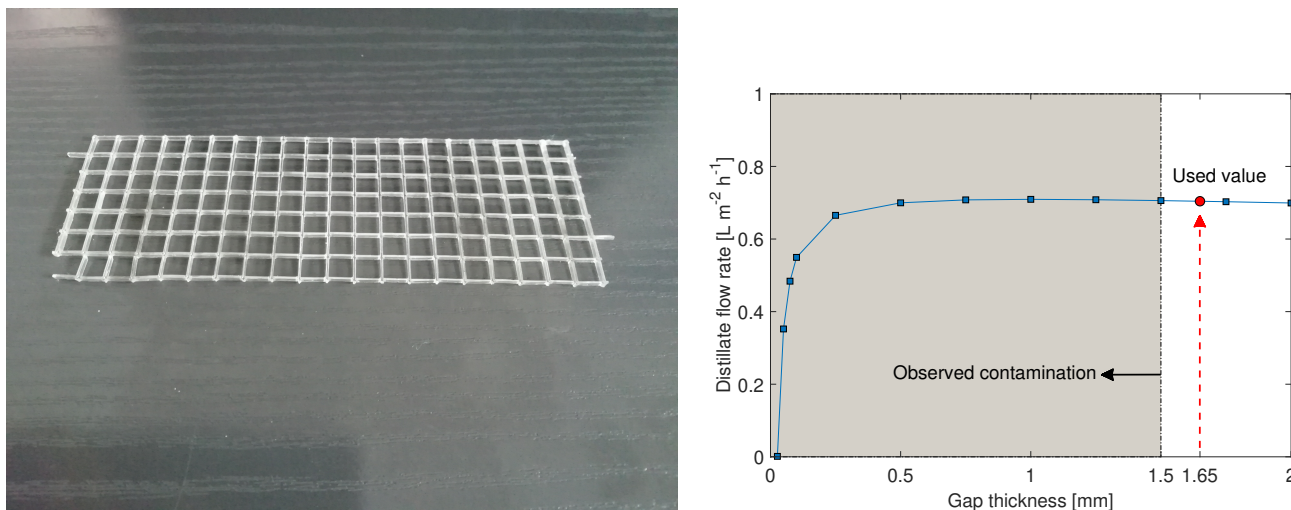


Figure S 6. Left-hand side: detail of the plexiglass spacer made with laser cutting. Right-hand side: modelling estimates of distillation performance as function of the air gap thickness as obtained by eqs. 28 and 29. A 1-stage configuration device fed with saltwater with NaCl concentration equal to 35 g L^{-1} is simulated. In the model, the considered equivalent solar irradiance is 950 W m^{-2} .

Even if the optimal value of the gap thickness in terms of distillate productivity reported in Supplementary Fig. S6 is $\approx 0.5\text{ mm}$, the effective thickness of the gap used for the experiments is higher than the predicted theoretical one, being equal to $1.65 \pm 0.05\text{ mm}$. This choice is necessary for avoiding contamination between evaporator and condenser. In fact, it is worth to point out that the gap has millimeter-sized pores (namely low liquid entry pressure values) and larger thickness values are necessary for being conservative and avoid contamination of distillate by the saltwater in the evaporating layer. Experiments showed that a 1.65 mm-thick gap is sufficient to avoid contamination in all the experiments carried out.

Perspectives. The theoretical model in eqs. 28 and 29 is exploited to estimate the performance of the device as function of the number of stages, air gap thickness and with two different solar absorber: black paint and selective absorber. The analysis is limited to a device with a maximum number of stages equal to 10, because of the limited capillary rise of the low-cost hydrophilic materials considered here.

When the black non selective absorber is considered, the optimal air gap thickness is $\approx 350 \mu\text{m}$, and the related productivity is $\approx 4 \text{ L m}^{-2} \text{ h}^{-1}$ in case of 10-stages configuration device (see black line in Supplementary Fig. S7, left-hand side).

When the selective absorber is installed, the optimal thickness is $\approx 500 \mu\text{m}$, and the related productivity is $\approx 6 \text{ L m}^{-2} \text{ h}^{-1}$ in case of 10-stages configuration device (see black line in Supplementary Fig. S7, right-hand side).

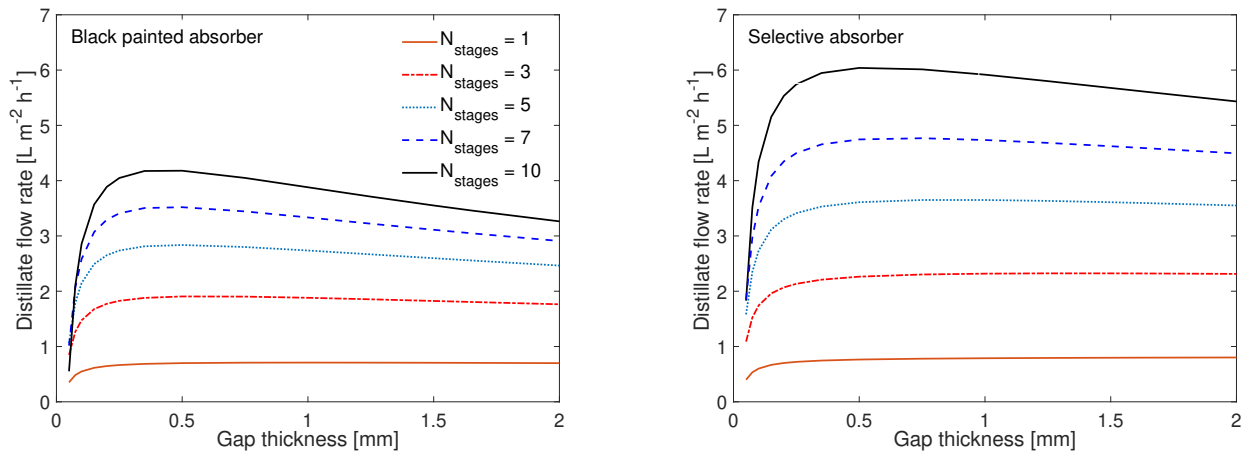


Figure S 7. Modelling estimates of optimized distillation performance in case of black absorber (left-hand side) and selective absorber (right-hand side). The effect of the number of stages and air gap thickness are explored by the model.

It is worth pointing out that, although the strength of the selective absorber is obviously the water yield due to the reduced radiative losses, a key parameter that should be also taken into account in practical application is the robustness and the long-term stability. The black absorber turned out to be more robust during tests, being less affected by deterioration when exposed to ambient (e.g. reduced optical performance after dust accumulation).

3.3 Thermal resistance of heat sink

A finned heat sink is placed below the last stage condenser, to efficiently dissipate the thermal energy flux into the environment and thus increase the temperature drop throughout the distillation device. An experimental procedure is used for evaluating its heat transfer coefficient (namely U). The employed experimental setup (see Supplementary Fig. S8) consists of 2 silicone heaters (57.6 ohms; francoCorradi) to provide a homogeneous and controllable heat flux. The 2 heaters reproduce the solar flux ($\approx 950 \text{ W m}^{-2}$) and are powered by a power supplier (PS 3003, HQ Power). Then, 3 K-type thermocouples RS Pro (2 applied on the top and 1 immersed in the basin, which acts as a thermostat) measure the temperature drop across the heat sink.

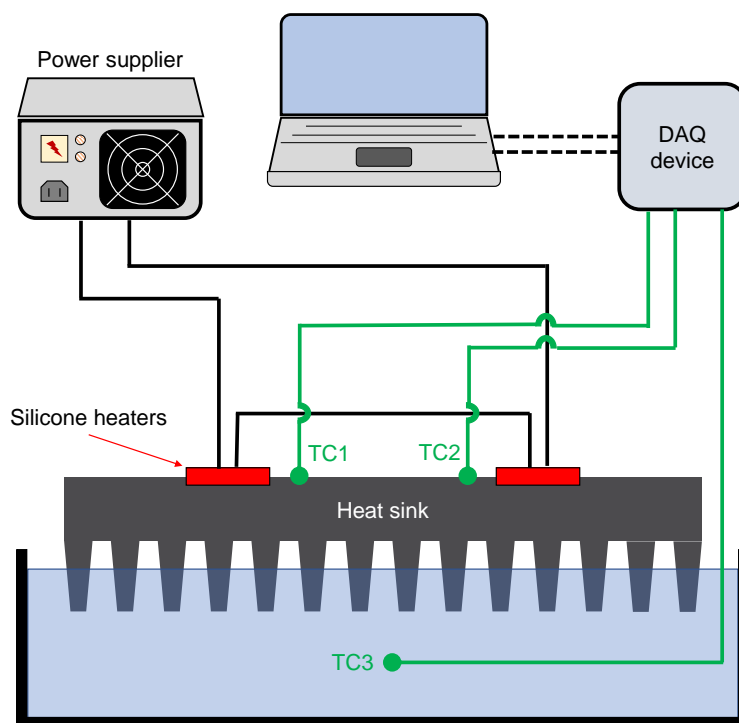


Figure S 8. Experimental setup for measuring the heat transfer coefficient of the heat sink. Thermocouples (TC) are represented by green lines.

In Supplementary Fig. S9, the temperature profiles, temperature drop and the effective heat transfer coefficient (namely $153 \text{ W m}^{-2} \text{ K}^{-1}$) are shown.

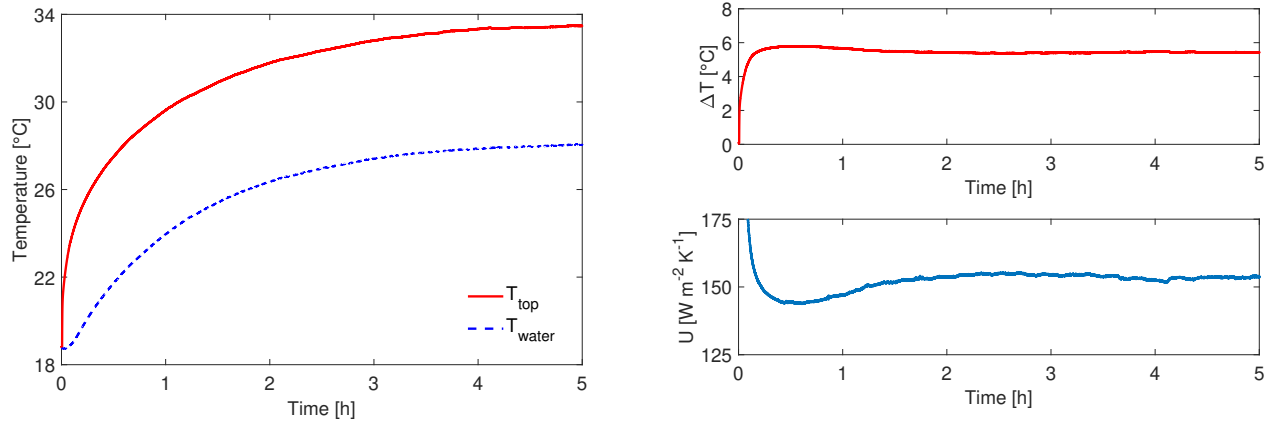


Figure S 9. Left-hand side: temperature profile during the characterization of the heat sink. Red line represents the average of the temperatures indicated with TC1 and TC2 in Supplementary Fig. S8 ($T_{top} = (TC1+TC2)/2$), whilst blue dashed line represents the temperature indicated with TC3 ($= T_{water}$) in Supplementary Fig. S8. Right-hand side: temperature drop ($\Delta T = (TC1+TC2)/2 - TC3$) across the heat sink (top panel, red line) and heat transfer coefficient (bottom panel, blue line).

3.4 Optical properties of solar absorber

Here, to reduce the cost, the aluminum foil placed on the top surface of the device is coated with Zynolyte[®] Hi-Temp aerosol spray paint. It is worth pointing out that the adopted aerosol-based solar absorber does not have optically selective properties, which would have ensured low emissivity in the infrared region and thus better thermal properties.

The coating is deposited with the same procedure extensively discussed by Cooper and co-workers. [6] In detail, five coating layers are first deposited. Then, the paint is dried at room temperature for 30 minutes and 2 heating cycles from room temperature to 250° C carried out.

To fully characterize its radiative losses, the emissivity of the aerosol-based black absorber is measured in the infrared region using an infrared camera (FLIR tg167). A thermocouple (Omega Engineering, 5TC-TT-K-40-36) is used to measure the temperature of the heated sample. Then, this value is compared with the temperature measured by the camera's sensor in order to infer the emissivity, which results to be ≈ 0.95 (see Supplementary Fig. S10).

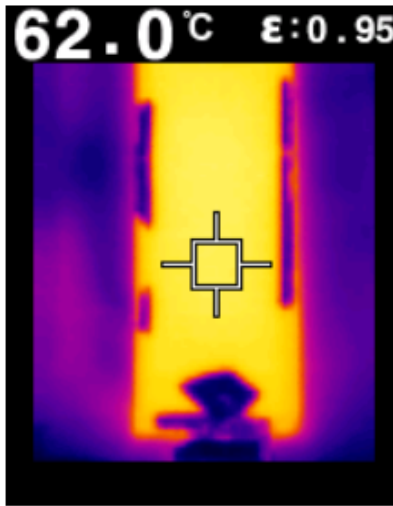


Figure S 10. Emissivity of the black absorber. Photo made with the infrared camera. The emissivity is evaluated at $\approx 62^\circ\text{C}$.

The result of emissivity found in our experiments is in good agreement with the value reported by Cooper and co-workers. [6] They determined the emittance of a similar material by measuring the infrared hemispherical reflectance spectrum via FTIR (Fourier Transform Infrared Spectroscopy). They found the spectral emittance to be relatively constant with an averaged value equal to 0.941 (minimum and maximum value equal to 0.9 and 0.97, respectively, over the range $2.5\ \mu\text{m}$ to $20\ \mu\text{m}$).

4 Supplementary Note: Productivity over time

The experimental productivity as function of time and its derivative are reported in Fig. S11. During daytime, the vapor generation from saltwater leads to salt accumulation in the hydrophilic layers used as evaporators. However, we did not observe the formation of any salt crust layer during the 8-hours tests of evaporation, which mimic a typical daylight duration. During these tests, the observed experimental performance already considers salt accumulation and its possible detrimental effect on evaporation; however, no appreciable decay in the evaporation rate has been noticed during the 8 hours of test.

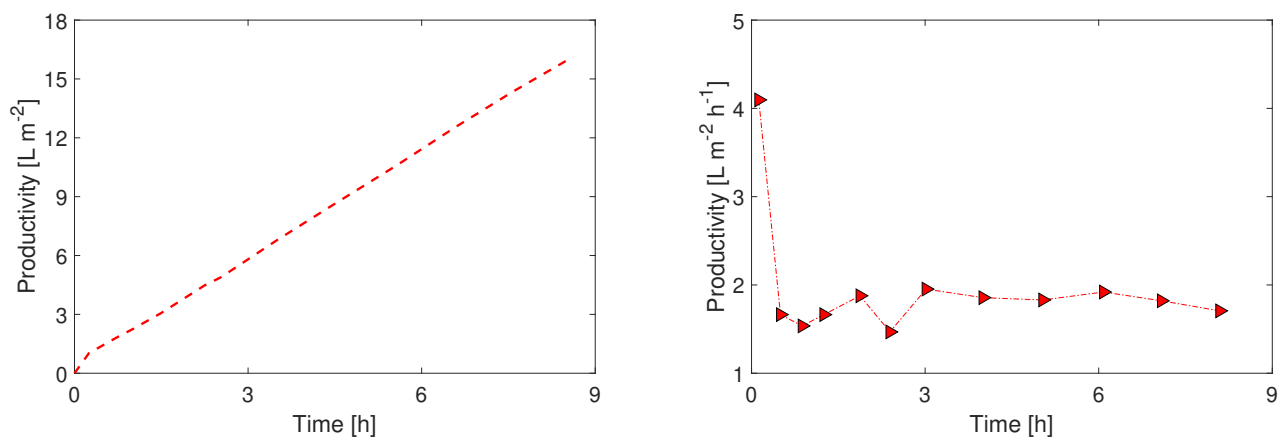


Figure S 11. Distillate production over time expressed as L m^{-2} (left-hand side) and its derivative expressed as $\text{L m}^{-2} \text{h}^{-1}$ (right-hand side). Without losing generality, here we report the productivity of the 3-stage configuration device.

5 Supplementary Note: Marangoni effect

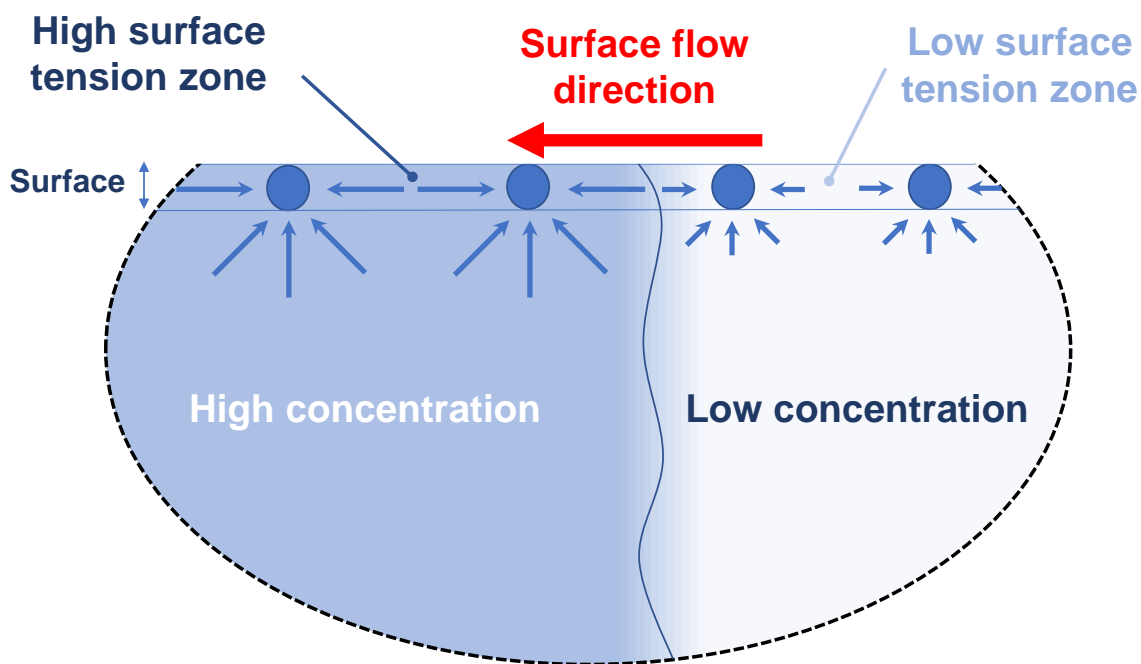


Figure S 12. Schematic of the Marangoni effect. The surface tension gradient is associated to a salt concentration gradient. The latter induces localized viscous stresses because of the resulting asymmetric interactions experienced by the molecules at the interface. Then, an interfacial flow, directed from the lower surface tension regions to the higher ones, takes place.

6 Supplementary Note: Salt rejection

6.1 Modeling the salt rejection from the evaporator

Fluid flow and transport of diluted species in porous medium. A finite element method is implemented to better interpret the salt rejection mechanism observed in the experiments. A two-dimensional model is developed by means of COMSOL Multiphysics®. In detail, the "Darcy Law" and the "Transport of diluted species" [7, 8] physics are employed. The simulations are performed under transient regime. The boundary conditions of the problem are summarized in Supplementary Fig. S13. It is worth pointing out that the 3D hydrophilic layer is reduced to a 2D geometry composed by 2 portions (on the same simulation plane): one without gravity effect (mimicking the hydrophilic layer used as evaporator, which is placed horizontally in the distillation device), and one where the gravitational force is applied (reproducing the strips through which the water is transported from the sea level up to the evaporator). An extremely fine mesh is employed and the Peclet number is ensured to be lower than four, for having convergence and stability.

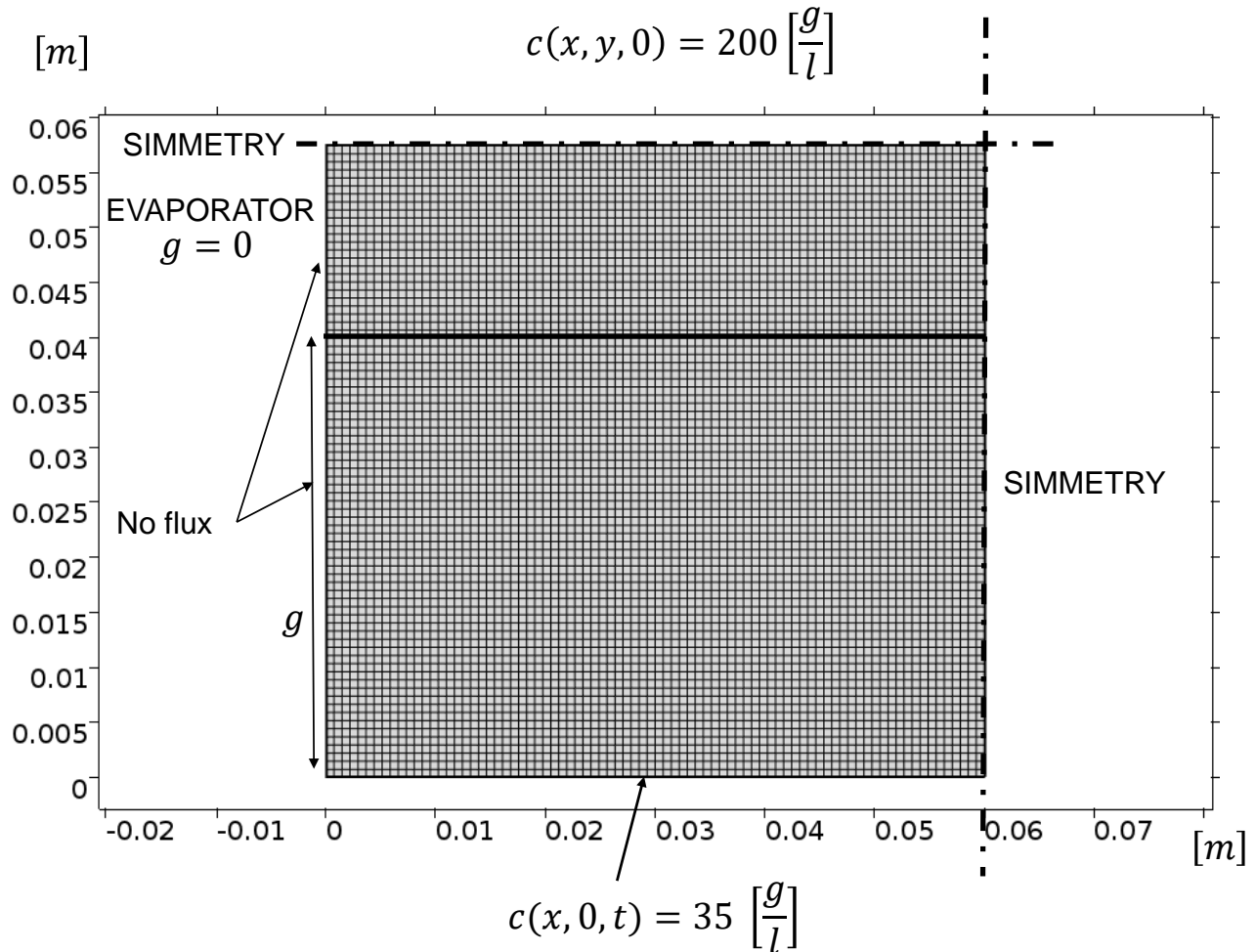


Figure S 13. Finite element model of the hydrophilic layer. The considered configuration is meshed by COMSOL Multiphysics® with 34820 degrees of freedom (plus 497 internal degrees of freedom). The transient process is simulated for 10 hours.

First of all, the solute (salt) is assumed to be inert, the fluid viscosity μ constant and the porous domain saturated by the solution, homogeneous and isotropic. The properties (namely, permeability k and porosity ϵ) of the latter are experimentally evaluated (see Supplementary Note 1). Due to strong interaction between the various physics involved in the model, the fully coupled

approach (generally used in multiphysics problems) is set. In fact, the problem involves total density variations of $\approx 20\%$, which makes this a strongly coupled flow case. [9]

The solution density ρ varies linearly with the solute concentration as follow:

$$\rho = \rho_0(1 + \gamma c), \quad (6)$$

where ρ_0 is the density of freshwater, $\gamma = \frac{\rho_s - \rho_0}{c_s - c_0}$ is the proportionality constant between concentration and density, c_0 and c_s are the salt concentrations of freshwater (namely 0 mol m^{-3}) and saturated salt water, respectively. ρ_s is the density of saturated salt water. The continuity equation applied to the porous medium (with ϵ porosity) is written as:

$$\frac{\partial(\epsilon\rho)}{\partial t} + \nabla \cdot (\rho\mathbf{u}) = 0, \quad (7)$$

being \mathbf{u} the fluid velocity. The momentum balance equation for variable density fluid flow in a porous medium, namely the Darcy's equation, can be written as follows:

$$\mathbf{u} = -\frac{k}{\mu}(\nabla p - \rho\mathbf{g}), \quad (8)$$

where k is the permeability ($1 \times 10^{-10} \text{ m}^2$, see Supplementary Note 3.1) of the porous medium. The gravity vector is $\mathbf{g} = (0, -g)$. The transport of diluted species in a porous medium is governed by the following advection-diffusion equation:

$$\epsilon \frac{\partial c_i}{\partial t} + \nabla \cdot \left(-\frac{\epsilon D_{eff,i}}{\tau_{wick}} \nabla c_i \right) + \mathbf{u} \nabla c_i = 0, \quad (9)$$

where c_i is the concentration of specie i (namely, mass of solute as a proportion of the total mass of solution), $D_{eff,i}$ is the effective diffusion coefficient and τ_{wick} is the tortuosity of the porous medium. Theoretically, both molecular and mechanical dispersion occur in solute transfer processes (the hydrodynamic dispersion coefficient is the sum of the molecular diffusion coefficient and mechanical dispersion coefficient). [10] Here, the hydrodynamic coefficient is only due to molecular diffusion, whilst the dispersion coefficient is neglected due to low velocities.

As far as the boundary conditions used in the described problem are concerned, no mass fluxes are considered through the sidewalls, which are therefore impermeable:

$$-\mathbf{n} \cdot \rho\mathbf{u} = 0 \quad (10)$$

$$-\mathbf{n} \cdot (-D_i \nabla c_i) = 0 \quad (11)$$

A Dirichlet boundary condition is applied at the bottom of the simulation domain to reproduce the fixed concentration of seawater (namely 35 g l^{-1} or 600 mol m^{-3}). On the other hand, the initial concentration of the horizontal portion of the evaporator is set to 200 g l^{-1} (namely 3450 mol m^{-3} , considering that the molecular weight of sodium chloride is 58.5 g mol^{-1}). The symmetry of the physics is exploited to reduce the computational cost of the simulation. Results are reported in Fig. 2a (see black dashed line).

Effective diffusion coefficient - Including Marangoni effect. In equation 9, a diffusion coefficient enhanced (namely $\approx 1.65 \times 10^{-7} \text{ m}^2 \text{ s}^{-1}$) with respect to the classical one (namely $\approx 1.5 \times 10^{-9} \text{ m}^2 \text{ s}^{-1}$ [11]) should be used to better mimic the salt rejection mechanism observed in the experiments. The discrepancy between the molecular diffusion coefficient under classical conditions and the effective one actually observed in the experiments is investigated and interpreted. As a matter of fact, an additional driving force for both the solvent and NaCl motion through the hydrophilic evaporator comes from the salt concentration gradient across the considered domain. In fact, this salt concentration gradient creates a surface tension gradient at the solution-air interface (see Supplementary Fig. S14), which gives rise to the so called Marangoni effect. [12]

Hence, to quantify the Marangoni effect acting in our distillation device, the effective diffusion coefficient used in equation 9 is evaluated by means of an additional COMSOL Multiphysics® simulation. The simulation domain (see Supplementary Fig. S15) consists of a saltwater thin film of thickness equal to 1 mm (namely the thickness of the hydrophilic layer, δ_l) and length equal to 1.75 cm (half of the horizontal portion of the evaporator). This simulation domain, which mimics the experiments presented in Fig. 2, is meshed by COMSOL Multiphysics® with 813564 degrees of freedom (plus 13187 internal degrees of freedom).

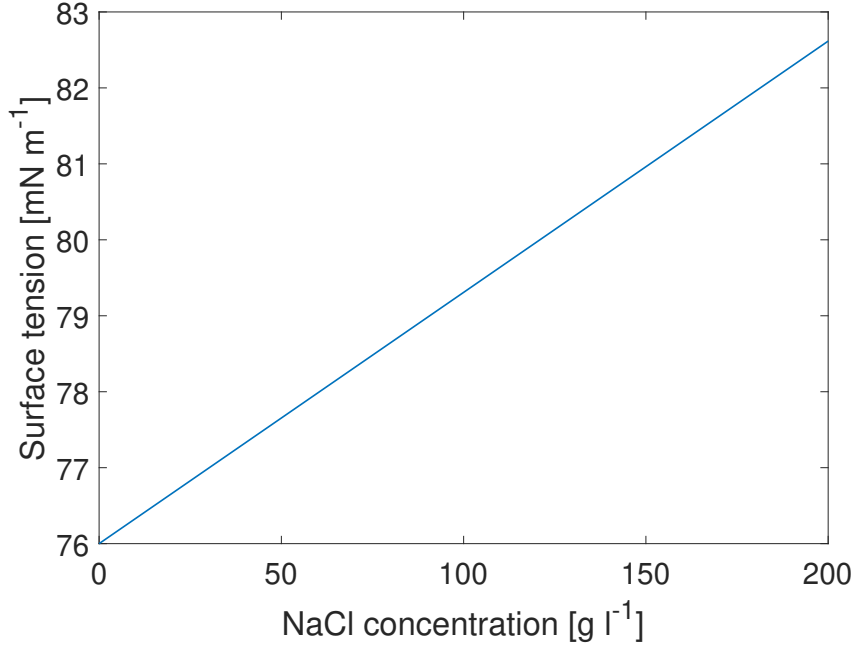


Figure S 14. Surface tension of aqueous NaCl solutions. [13, 14]

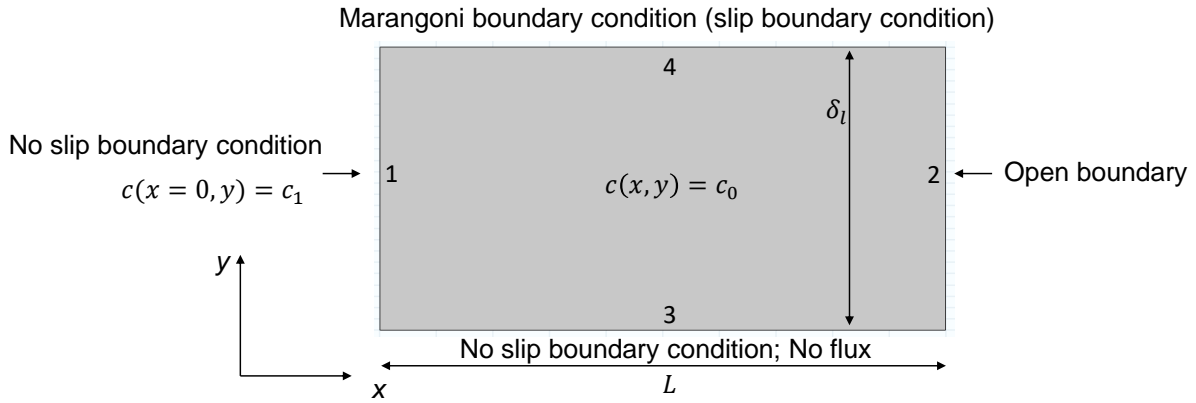


Figure S 15. Simulation domain and boundary conditions employed to quantify Marangoni effect in the evaporating layer. Note that, for the sake of clarity, the simulation domain is not in scale.

Two sets of equations are solved numerically to investigate the diffusion phenomenon in presence of a solution-air interface (see boundary 4 in Supplementary Fig. S15). In detail, "Laminar flow" and "Transport of diluted species" [7, 8] are coupled and solved. In the model, the Navier-Stokes equation is written as:

$$\mathbf{u} \cdot \nabla \rho \mathbf{u} = -\nabla p + \nabla \cdot \left(\mu (\nabla \mathbf{u} + (\nabla \mathbf{u})^T) - \frac{2}{3} \mu (\nabla \cdot \mathbf{u}) \mathbf{I} \right) \quad (12)$$

where μ is the viscosity of the solution. The boundary conditions reported in Supplementary Fig. S15 are applied. In detail, a Dirichlet boundary condition is applied at the left side of the simulation domain (labeled as 1) to reproduce a fixed arbitrary concentration of NaCl (c_1). On the other hand, the initial concentration of the entire domain is set to c_0 equal to 35 g l^{-1} (namely the seawater concentration). Then, no slip boundary condition (namely $\mathbf{u}=0$) is applied at boundaries 1 and 3 (because of the contact of the hydrophilic layers with a not moving wall, namely the support), and an open boundary condition is applied on 2.

The latter can be formalized as follows:

$$c = c_0, \text{ if } \mathbf{u} \cdot \mathbf{n} < 0 \quad (13)$$

$$-\mathbf{n} \cdot (-D_i \nabla c_i) = 0, \text{ if } \mathbf{u} \cdot \mathbf{n} \geq 0 \quad (14)$$

Note that the no flux boundary condition applied on boundary 3 is equivalent to eqs. 10 and 11. Finally, a slip condition is applied on the boundary labeled as 4 to reproduce the velocity at the surface under the existence of surface tension gradient, namely Marangoni effect:

$$[-p\mathbf{I} + \mu(\nabla \mathbf{u} + (\nabla \mathbf{u})^T) - \frac{2}{3}\mu(\nabla \cdot \mathbf{u})\mathbf{I}]\mathbf{n} = \sigma \nabla c \quad (15)$$

where $\sigma \approx 1.76 \times 10^{-6} \frac{\text{N m}^{-1}}{\text{mol m}^{-3}}$ is the concentration derivative of the surface tension γ (namely $\sigma = \frac{\partial \gamma}{\partial c}$). Note that the pressure is set to 1 atm at the outlet section (boundary labeled as 2).

The simulation results are reported in Supplementary Fig. S16.

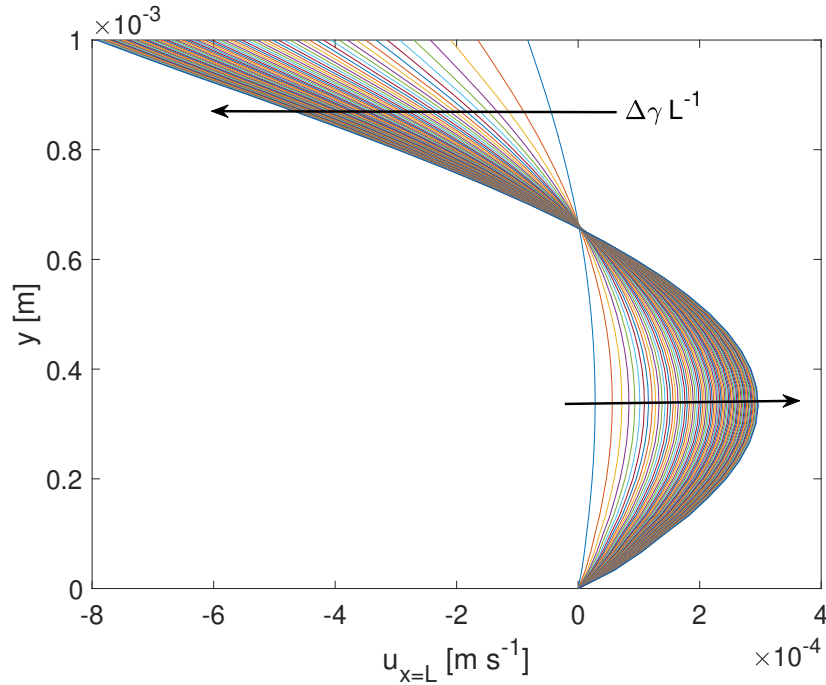


Figure S 16. Stationary velocity profiles of the saltwater solution in case of Marangoni effect. The profiles are evaluated at the outlet section ($x = L$). The minimum and the maximum values of the concentration of the saltwater solution are 35 and 200 g l^{-1} , respectively.

The stationary velocity profiles at the outlet section ($x = L$) are reported as function of the driving force (Marangoni effect), which depends on the concentration c_1 applied on boundary 1, namely $\Delta \gamma L^{-1} = \sigma \Delta c L^{-1} = \sigma (c_1 - c_0) L^{-1}$. The back flow is due to the slip condition at the water-air interface (boundary labeled as 2 in Supplementary Fig. S15) together with the no-slip condition at the sidewall labeled with 1 in Supplementary Fig. S15.

The transient concentration surface plots after 5 seconds, 5 minutes and at stationary conditions are reported in the main text (see Fig. 2c). In Fig. 2c (left side), the results of a classic diffusion mechanisms are represented. On the other hand, simulation results obtained by including the Marangoni effect (see equation 15) are shown in Fig. 2c (right side).

We stress that the fluid flow in the subsurface is considered to be a continuum process, where average bulk properties are used instead of considering a pore-scale flow. In the latter case, the shape and the orientation of the interstices should be also taken into account. For example, scanning electron microscope could provide images of a sample of the hydrophilic layer to simulate the exact geometry of the domain, thus reproducing a more realistic flow.

Finally, it is worth pointing out that – in case of classic molecular diffusion – the order of magnitude of the diffusion velocity is $\frac{D}{\delta_l} \approx 10^{-6} \text{ m s}^{-1}$ and the related Reynolds number $\frac{\rho u \delta_l}{\mu} \approx 10^{-3}$. This means that creeping flow occurs and Navier-Stokes equation could be replaced by Stokes equations. On the other hand, considering the slip boundary condition applied on boundary

4 (Marangoni effect), the resulting Reynolds number increases up to $\approx 10^{-1}$ and Navier-Stokes equation have to be used to solve the laminar flow.

6.2 Theoretical analysis of Marangoni effect

The fluid flow that takes place in case of Marangoni effect and the associated velocity are evaluated by reducing and analytically solving the Navier-Stokes equations. The imposed boundary conditions are consistent with the ones already used in the numerical analysis reported in Supplementary Note 6.1. In detail, to reduce the complexity of the equations we assume that the width (W) and length (L) of the hydrophilic layer are sufficiently larger with respect to the depth (δ_l). Also, we assume that the density and concentration gradient along x direction are fixed (see Supplementary Fig. S15) and that the flow is incompressible.

The governing continuity and momentum equations, in case of steady-state conditions and 2 dimensional fluid flow, are outlined as follows:

$$\frac{\partial u_x}{\partial x} + \frac{\partial u_y}{\partial y} = 0 \quad (16)$$

$$\rho u_x \frac{\partial u_x}{\partial x} + \rho u_y \frac{\partial u_x}{\partial y} = -\frac{\partial p}{\partial x} + \mu \left(\frac{\partial^2 u_x}{\partial x^2} + \frac{\partial^2 u_x}{\partial y^2} \right) \quad (17)$$

$$\rho u_x \frac{\partial u_y}{\partial x} + \rho u_y \frac{\partial u_y}{\partial y} = -\frac{\partial p}{\partial y} + \mu \left(\frac{\partial^2 u_y}{\partial x^2} + \frac{\partial^2 u_y}{\partial y^2} \right) \quad (18)$$

Further, the term $\frac{\partial u_x}{\partial x}$ is much smaller than $\frac{\partial u_x}{\partial y}$, because $\frac{\delta_l}{L} \ll 1$. The reduced ratio $\frac{\delta_l}{L}$ leads us to safely approximate $u_y = 0$. Thus, the eqs. 16, 17 and 18 are reduced to:

$$\frac{\partial p}{\partial x} = \mu \left(\frac{\partial^2 u_x}{\partial y^2} \right), \quad (19)$$

which can be integrated obtaining:

$$u_x = y^2 \frac{\partial p}{\partial x} \frac{1}{2\mu} + C_1 y + C_2. \quad (20)$$

First, the no-slip boundary condition at the bottom part of the domain (i.e. the support of the hydrophilic strip) gives us the integration constant C_2 :

$$u_x(y = 0) = 0 \rightarrow C_2 = 0. \quad (21)$$

Second, the slip condition responsible of the velocity at the fluid-air interface provided by the surface tension gradient (Marangoni effect) is used to figure out the integration constant C_1 :

$$\frac{\partial \gamma}{\partial x} = \mu \frac{\partial u_x}{\partial y} \Big|_{y=\delta_l} \rightarrow C_1 = \frac{1}{\mu} \frac{\partial \gamma}{\partial x} - \frac{\delta_l}{\mu} \frac{\partial p}{\partial x}. \quad (22)$$

An additional condition is necessary to correlate the pressure gradient and the surface tension gradient: since the fluid is assumed as incompressible and at steady state, the continuity equation implies that the average velocity over the saltwater thin film cross-section should be equal to zero, that is

$$\frac{1}{\delta_l} \int_0^{\delta_l} u_x dy = 0 \rightarrow \frac{\partial p}{\partial x} = \frac{3}{2} \frac{1}{\delta_l} \frac{\partial \gamma}{\partial x}. \quad (23)$$

The final expression for the fluid velocity along the x axis is:

$$u_x = y^2 \frac{3}{4\delta_l \mu} \frac{\partial \gamma}{\partial x} - \frac{1}{2\mu} \frac{\partial \gamma}{\partial x} y. \quad (24)$$

We stress that the analytical formulation is based on the assumption that $u_x \frac{\partial u_x}{\partial x}$ is much smaller than $\frac{\mu}{\rho} \frac{\partial^2 u_x}{\partial y^2}$ and then is only valid when:

$$\frac{\Delta\gamma}{L} \ll \frac{4\mu^2 L}{\rho\delta_l^3}. \quad (25)$$

Considering our geometry ($L = 1.75$ cm and $\delta_l = 1$ mm) and operating parameters, the term at the right hand side of equation 25 is ≈ 0.1 Pa (this threshold value is indicated as Γ_{th}). In Supplementary Fig. S17, the analytical velocity profiles (red curves) are compared with the ones obtained by means of COMSOL simulations (blue dashed lines) at different values of $\Delta\gamma L^{-1} = \Gamma$ (namely 1×10^{-4} Pa, 2×10^{-4} Pa, 5×10^{-4} Pa and 1×10^{-3} Pa, which correspond to salinity gradients $\approx 3.3, 6.6, 16.5$ and $33 \text{ g l}^{-1} \text{ m}^{-1}$, respectively).

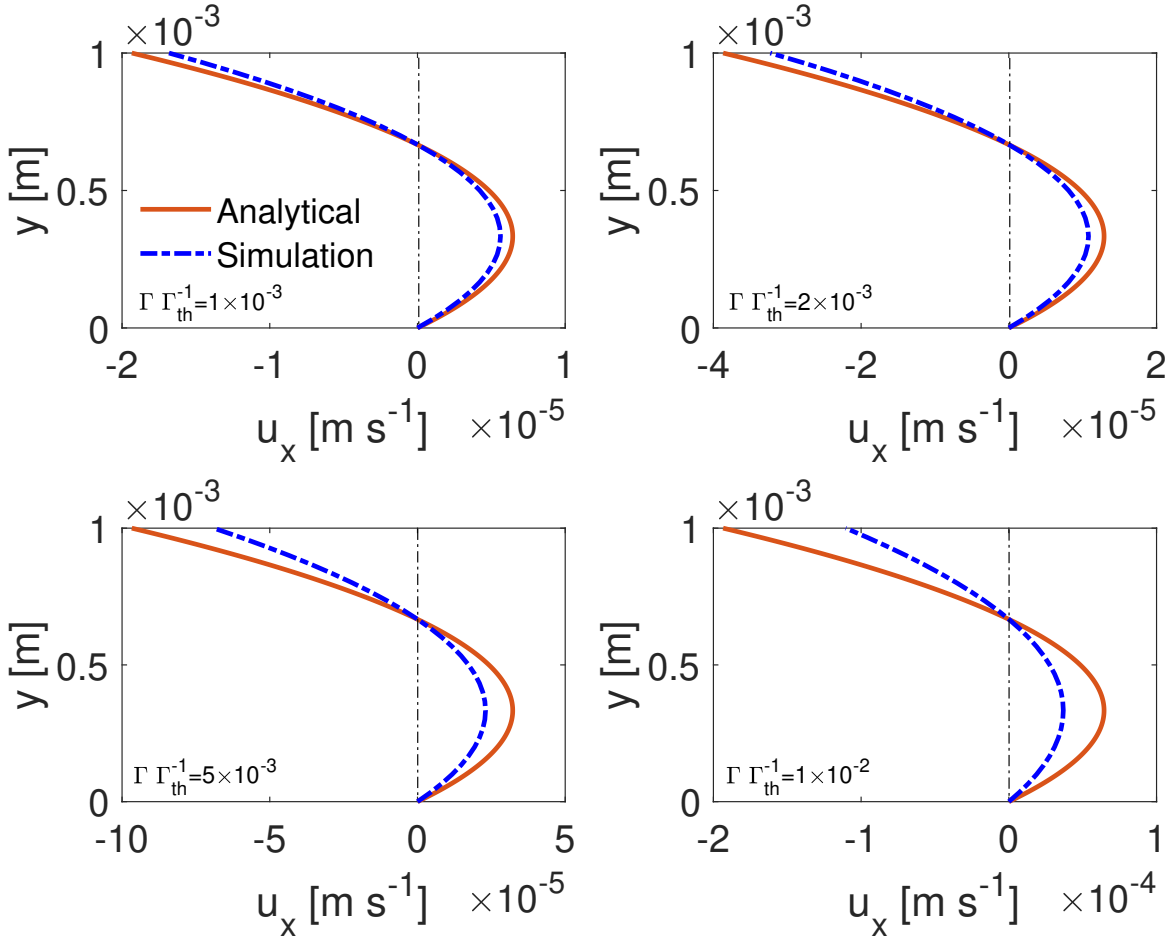


Figure S 17. Comparison between analytical (red lines; eq. 24) and numerical (blue dashed lines) velocity profiles.

7 Supplementary Note: Distillation performance of the prototype in laboratory conditions

The measurements are carried out at Massachusetts Institute of Technology and Politecnico di Torino to prove the reproducibility of results. The experimental setup is represented in Supplementary Fig. S18.

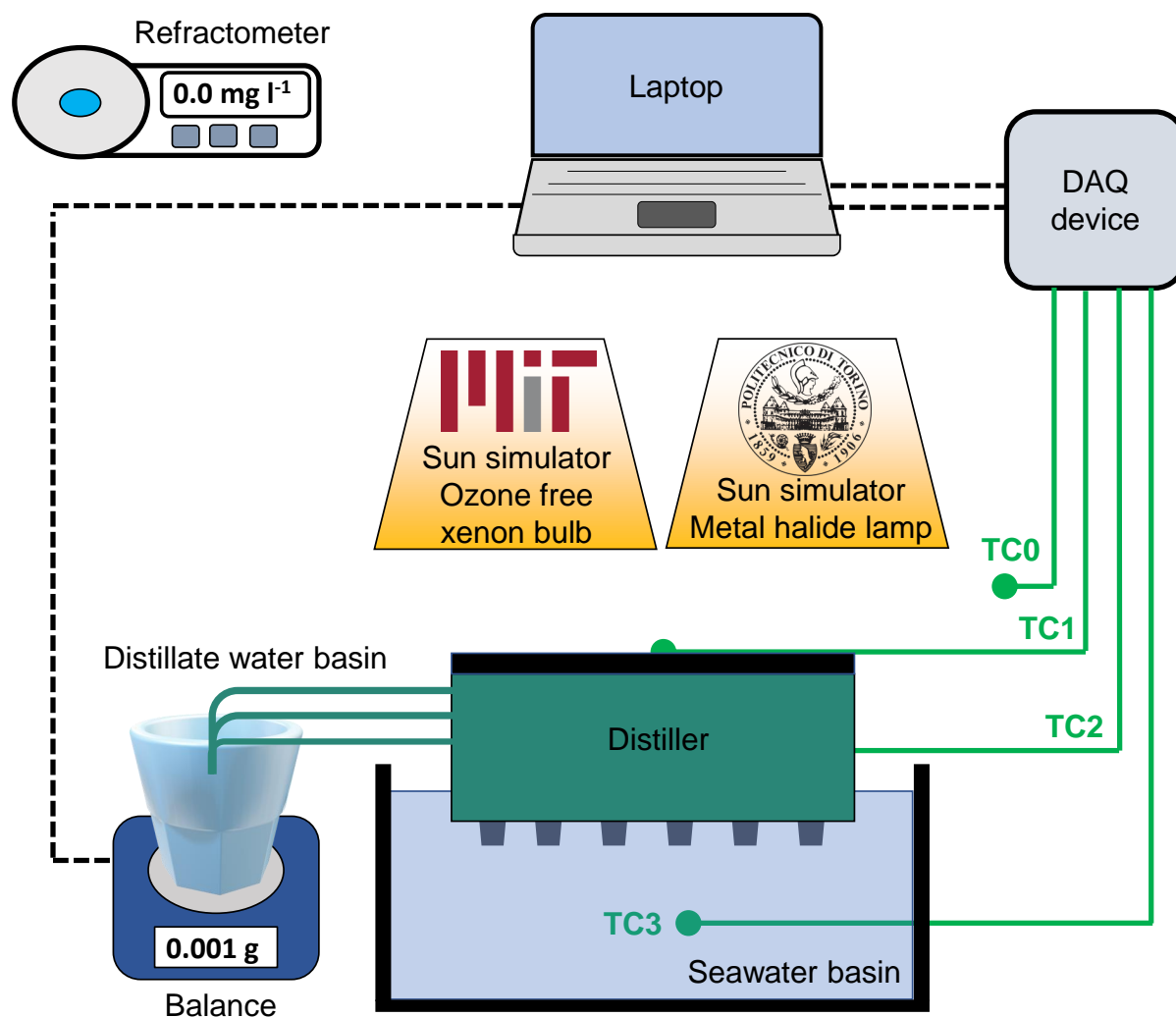


Figure S 18. Laboratory testing of the modular distiller. The experimental tests carried out under laboratory conditions include the following components: (1) a laptop for data storage and elaboration, (2) a data acquisition board, (3) a refractometer for salinity measurement, (4) two different sun simulators (the one installed at MIT and the one installed at Politecnico di Torino), (5) a balance for distillate mass measurement, (6) an output basin for the distilled water, (7) an input basin for the saltwater, and (8) the modular distiller. The temperatures of the ambient and seawater in the basin are measured with TC0 and TC3 thermocouples, respectively; the temperatures of the black absorber and last stage condenser are measured with TC1 and TC2 thermocouples, respectively.

A sun simulator is used to properly reproduce the entire solar spectrum and test the passive distiller. The device is placed in a glass basin containing up to 5 liters of artificial NaCl solution (salinity equal to 35 g L^{-1}). Due to the large amount of seawater in the basin with respect to the distillate productivity, the salt concentration does not significantly change during operating conditions. The distillate flow rate gathered in the distillate water basin is measured by a balance (see Supplementary Fig. S18 and S.19). Steady-state productivities are measured for up to 8 hours of continuous operations.

Experiments	J [L m ⁻² h ⁻¹]	R-square
1 (MIT)	0.779	0.985
2 (MIT)	0.695	0.993
3 (MIT)	0.706	0.991
4 (MIT)	0.802	0.997

Table S 2. Distillate flow rate achieved testing the 1-stage configuration device. All the experiments were carried out at MIT. R-square is evaluated using the Bisquare method.

Experiments	J [L m ⁻² h ⁻¹]	R-square
1 (MIT)	1.902	0.997
2 (MIT)	1.973	0.999
3 (Polito)	1.608	0.996
4 (Polito)	2.133	0.981

Table S 3. Distillate flow rate achieved testing the 3-stage configuration device. Experiments were carried both at MIT and Politecnico di Torino. R-square is evaluated using the Bisquare method.

The experimental setup used at MIT [2] employs a ScienceTech, SS-1.6K sun simulator (see Supplementary Fig. S19). The solar flux is measured using a thermopile (Newport, 818P-040-55, spectral range 0.19 to 11 μm) connected to a calibrated power meter (Newport, 1918-C). The measured value of solar flux is obtained by averaging five measures from different locations covering the entire area occupied by the device. Several thermocouples (Omega Engineering, 5TC-TT-K-40-36) are installed in the experimental setup and recorded using an Omega Engineering DAQPRO. An analog refractometer (accuracy $\pm 0.2\%$) is used to measure the salinity of the solutions. The testing facilities used at Politecnico di Torino consist of a infinityPV ISOSun solar

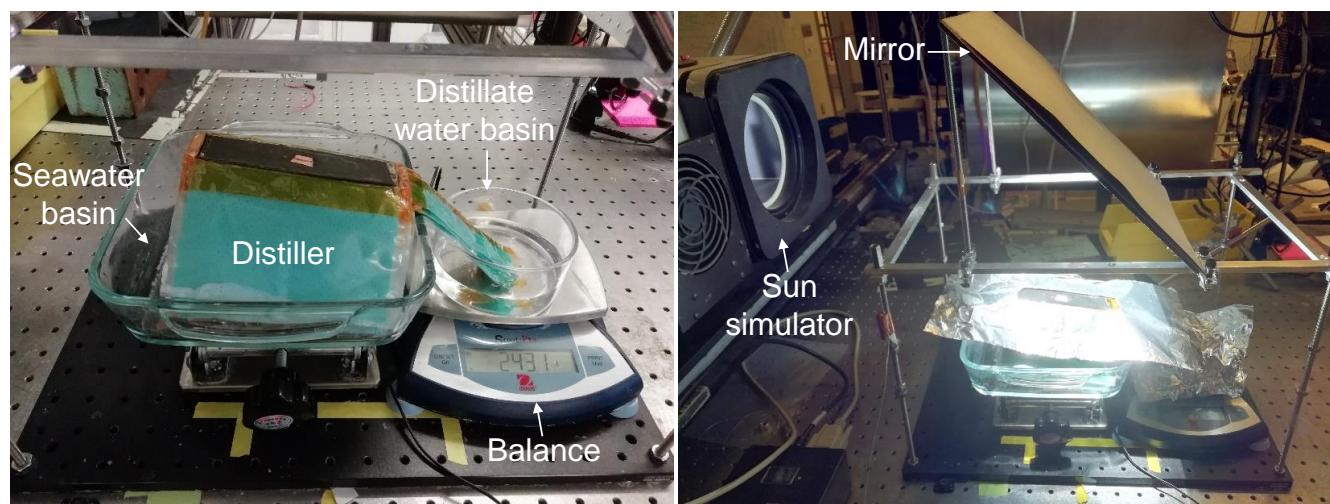


Figure S 19. Pictures of the experimental setup used at MIT.

simulator [15] (maximum deviation over the area $<\pm 5\%$ and $<\pm 1\%$ in the central testing area; stability in time $<\pm 1\%$ at 1000 W m^{-2} over 24 hours), a laptop for data storage and analysis, a data acquisition board (NI-9213 module for DAQ board, National Instruments), a digital refractometer (HI 96801 Hanna Instruments, accuracy $\pm 0.2\%$), a precision scale (Kern PCB 1000-2, 0.01 g resolution) and a pyranometer (LP Pyra 08 BL; Delta OHM). K-type thermocouples (RS Pro) are connected with the DAQ board.

With both the experimental setups, the imposed solar flux is equal to 950 W m^{-2} . Then, the temperature of the black coating (absorber), last condenser (namely the last hydrophilic layer interfaced with the heat sink), seawater basin, and ambient are recorded. Thermocouples are placed at the center of the black coating and of the hydrophilic layer to reduce side effects.

In case of 1-stage configuration device, the results of the four experiments are summarized in Table 2, whilst in case of 3-stages configuration device the performance are summarized in Table 3.

For the sake of completeness, a comparison between the performance achieved with the sub-optimal version of the device [1] and the improved version developed in this work is carried out to validate that the experimental setup employed in this work provides results coherent with previous observations. [1]

Under the sun simulator installed at Polito, the first version of the distiller shows the same performance (see Supplementary Fig. S20) published in our previous work [1], namely distillate productivity equal to $1.468 \text{ L m}^{-2} \text{ h}^{-1}$ over 8 working hours tested with 900 W m^{-2} (maximum discrepancy with the previous results reported ref. [1] equal to 1.8%), therefore validating the experimental protocol adopted in this work. The temperature profiles are shown in Supplementary Fig. S20.

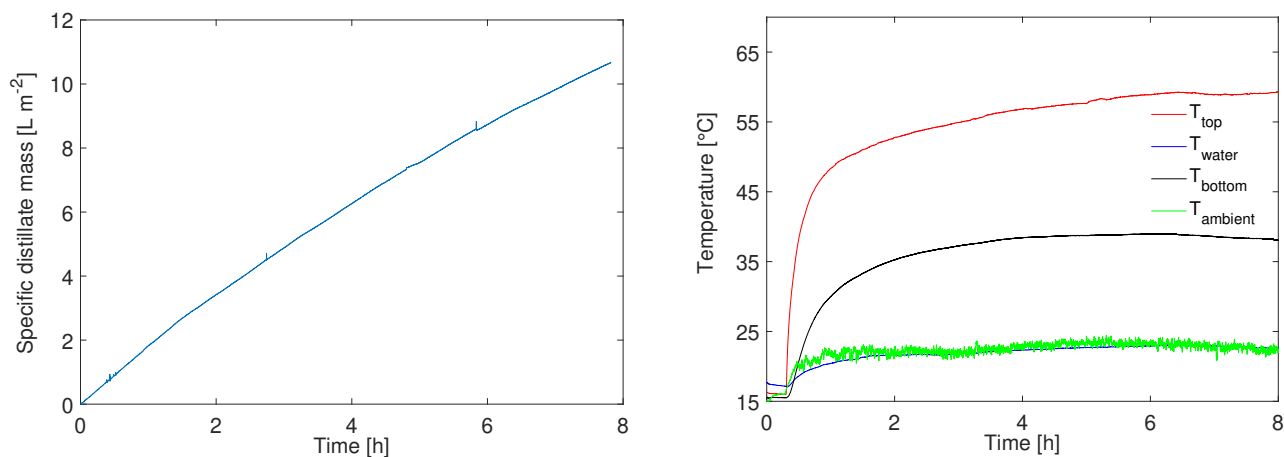


Figure S 20. Desalination performance of the version of the 3-stage distiller reported in ref. [1], tested under the sun simulator at Polito. The device is tested under laboratory conditions, with 900 W m^{-2} input thermal energy. Temperature profiles of the distiller tested under the sun simulator are reported as well. Red, black, blue and green lines represent the first stage evaporator (top side of the distiller), last stage condenser (bottom side of distiller), water and ambient temperatures, respectively.

8 Supplementary Note: Theoretical model for distillation process

The theoretical model introduced and extensively discussed in ref. [1] for predicting the distillation performance of the device is exploited to interpret the experimental results. Then, based on the same assumptions and considering a configuration where only an air gap (with normalized effective area γ_{spacer}) of thickness d_a and $\tau = 1$ is located between evaporator and condenser, the Maxwell-Stefan and Dusty gas model can be simplified as:

$$-\frac{dx_w}{dz} = \frac{(1-x_w)N_w}{\frac{P\gamma_{spacer}D_{wa}}{TR}} \quad (26)$$

where x_w is the mole fraction of water vapour, z is the vertical coordinate, N_w is the molar flux of water vapour, P is the total pressure of the mixture, D_{wa} is the diffusion coefficient of water vapour in air, T is the absolute temperature and R is the gas constant ($8.314 \text{ J K}^{-1} \text{ mol}^{-1}$).

Then, equation 26 can be integrated within the air gap, considering as boundary conditions $x_w^E = \frac{a(Y_E)p_v(T_E)}{P}$ when $z = z_E$ (evaporator side), $x_w^C = \frac{a(Y_C)p_v(T_C)}{P}$ when $z = z_C$ (condenser side). Note that a denotes the activity of water, Y_E and Y_C are the mass fractions ($Y = m_{salt}/m_{solution}$) of salt in the feed and distilled solution, respectively and p_v is the water vapour pressure.

Within the air gap thickness, where the diffusion mechanism is only due to molecular diffusion, the equation is:

$$-\int_{z_E}^{z_C} \frac{dx_w}{1-x_w} = \int_{z_E}^{z_C} \frac{N_w dz}{\frac{P\gamma_{spacer}D_{wa}}{TR}} \quad (27)$$

which yields:

$$J = C \ln \left(\frac{1-x_w^C}{1-x_w^E} \right), \quad (28)$$

where $J = M_{H_2O}N_w$ is the specific mass flow rate of the distillate through the stage, M_{H_2O} is the molar mass of water (expressed as kg mol^{-1}) and $C = \frac{M_{H_2O}P\gamma_{spacer}D_{wa}}{RTd_a}$. Note that it is possible to empirically estimate $PD_{wa} = 1.19 \times 10^{-4} T^{1.75}$, expressed as $\text{Pa m}^2 \text{ s}^{-1}$. [16]

In each stage of the distiller, the specific heat flux (q , W m^{-2}) between the evaporating and condensing hydrophilic layers is due to water phase change and heat transfer by conduction, namely

$$q = \frac{k_{eff,g}}{d_g} (T_E - T_C) + J\Delta h_{LV} + q_l, \quad (29)$$

where $k_{eff,g}$ is the effective thermal conductivity in the gap, including conduction through the air and spacer; T_E and T_C are the temperatures of the feed and permeate solution, respectively; Δh_{LV} is the latent heat of vaporization; q_l is the specific heat loss through the lateral surface of the stage.

Setup	h [$\text{W m}^{-2} \text{K}^{-1}$]	γ_{spacer} [-]	ϵ_{spacer} [-]	d_a [mm]	T_{sky} [K]
Laboratory	$2.5 \div 7.5$	$0.576 \div 0.910$	$0.74 \div 0.87$	$1.6 \div 1.7$	295
Roof	$7 \div 10$	$0.576 \div 0.910$	$0.74 \div 0.87$	$1.6 \div 1.7$	263

Table S 4. Uncertainties in the theoretical model. Upper and lower values of the variable considered in the theoretical model determine the uncertainty of model estimations: h , convective heat transfer coefficient (distiller-ambient); γ_{spacer} and ϵ_{spacer} , normalized effective area and porosity of the air gap, respectively; T_{sky} , sky temperature for radiative heat losses. As far as h is concerned, the upper and lower values represent the typical convective heat transfer coefficients for air under natural convection regime. The upper (mean value + 1 s.d.) and lower (mean value - 1 s.d.) values of γ_{spacer} and ϵ_{spacer} are inferred from experimental evidences.

9 Supplementary Note: Cost estimation

An estimate of the cost breakdown of various components of the device is carried out using prices of similar items found on a online wholesale market (Alibaba.com). The tested 3-stage configuration devices are considered, comparing the cost of the proposed distiller with the one reported in ref. [1].

As far as the distiller described in ref. [1] is concerned, the lab-scale prototype cost is ≈ 6.6 USD. In detail, the hydrophobic PTFE membrane counts for 20% of the cost, followed by the aluminum sheets for preventing contamination (6%), by the hydrophilic microfiber wicks (3.5%), by the selective absorber (1.5%), by the 3D printed convection reducer (15%) and by the heat sink (54%). Then, based on a two-years lifetime, the desalinated water cost is ≈ 52 USD m^{-3} .

Note that, for the sake of simplicity, the following cost contributions are neglected: polystyrene floating element, auxiliaries (hydraulic/mechanical fittings), distilled basin and pumps for distillate evacuation.

As discussed, in the current distiller, the selective absorber is substituted by a more robust aerosol-based black paint and the 3D printed convection reducer is removed. In addition, the membrane is substituted with a plexiglass spacer that creates the air gap between the evaporator and the condenser. Therefore, the bill of materials includes the hydrophilic layers (fabrics), heat sink, plexiglass frame (namely PMMA) and the aluminum sheets for preventing contamination. The cost of each part is summarized below:

- hydrophilic layers: 2 USD m^{-2} , quantity used ≈ 0.06 m^2 (cost 0.12 USD, which covers 10% of the total cost);
- heat sink: 250 USD m^{-2} (cost ≈ 1 USD, which covers 79.3% of the total cost);
- plexiglass frame: 2.8 USD m^{-3} , quantity used ≈ 20 grams (cost 0.056 USD, which covers 5.2% of the total cost);
- aluminum sheets: 2.5 USD kg^{-1} , quantity used ≈ 10 grams (cost 0.025 USD, which covers 5.5% of the total cost).

It is worth pointing out that the weight of the plexiglass, and as consequence its cost, considers a bulk sheet and includes the weight of the scraps too. In addition, the cost of the aerosol-based paint is neglected due to the low value and to the difficulty in estimating the used quantity for each device. The total cost of the tested device is then ≈ 1.3 USD. In Supplementary Fig. S21, the estimated total cost of the distiller reported in ref. [1] and the current one are summarized, together with the detailed cost of each component. Note that the cost of the device can be further reduced by removing the heat sink, which is the most expensive component, and operating by means of natural convection.

Considering the productivity experimentally obtained with the 3-stage configuration device (namely 1.9 L $m^{-2} h^{-1}$) and two years lifetime, the estimated water production cost is about 26 USD m^{-3} that means a cost reduction, with respect to the first version of the distiller, equal to 50%.

For the sake of completeness, a 10-stage configuration device is considered too. A distillate productivity is extrapolated from the model in which the optimal thickness of the gap and a selective absorber are taken into account. In this case, the cost of the device would be 1.85 USD (here, the various contributions to the total cost are: 14% aluminum, 24% hydrophilic layers, 4% plexiglass frame, 57% heat sink and 1% selective absorber). The predicted productivity is ≈ 6 L $m^{-2} h^{-1}$, which means a cost of 12 USD m^{-3} . Two years lifetime is considered.

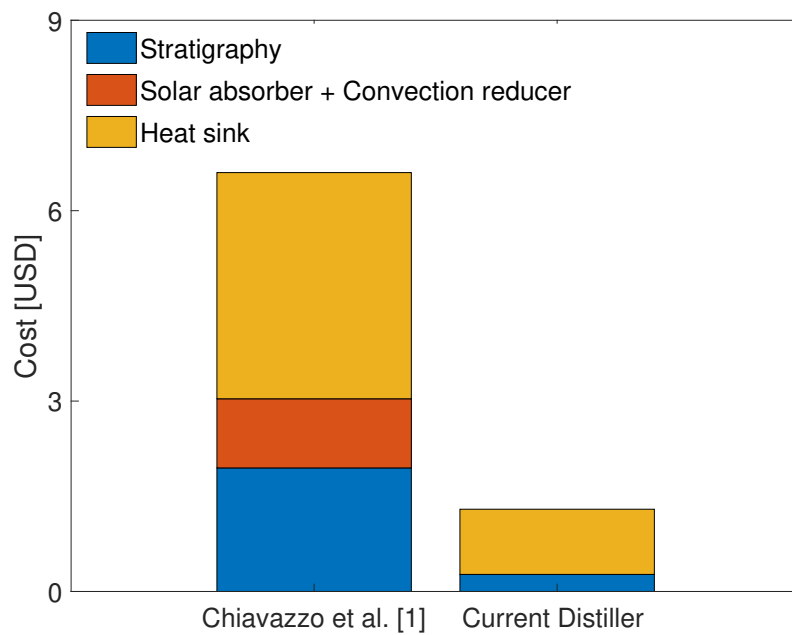


Figure S 21. Estimated cost of distillers and their various components. Costs are referred to 2019. The 3-stage configuration device is considered. Note that, the "stratigraphy" cost contribution includes the hydrophilic layers, aluminum sheets and membrane (in case of the device reported in ref. [1]) or plexiglass frame (in case of the current distiller).

References

- [1] Eliodoro Chiavazzo, Matteo Morciano, Francesca Viglino, Matteo Fasano, and Pietro Asinari. Passive solar high-yield seawater desalination by modular and low-cost distillation. *Nature Sustainability*, 1(12):763, 2018.
- [2] George Ni, Seyed Hadi Zandavi, Seyyed Morteza Javid, Svetlana V. Boriskina, Thomas A. Cooper and Gang Chen. A salt-rejecting floating solar still for low-cost desalination. *Energy & Environmental Science*, 11(6):1510–1519, 2018.
- [3] Yuehua Yuan and T. Randall Lee. Contact angle and wetting properties. In *Surface science techniques*, pages 3–34. Springer, 2013.
- [4] Daniel J. Preston, Kyle L. Wilke, Zhengmao Lu, Samuel S. Cruz, Yajing Zhao, Laura L. Becerra and Evelyn N. Wang. Gravitationally driven wicking for enhanced condensation heat transfer. *Langmuir*, 34(15):4658–4664, 2018.
- [5] Akshay Deshmukh and Menachem Elimelech. Understanding the impact of membrane properties and transport phenomena on the energetic performance of membrane distillation desalination. *Journal of Membrane Science*, 539:458–474, 2017.
- [6] Thomas A. Cooper, Seyed Hadi Zandavi, George W. Ni, Yoichiro Tsurimaki, Yi Huang, Svetlana V. Boriskina and Gang Chen. Contactless steam generation and superheating under one sun illumination. *Nature communications*, 9(1):5086, 2018.
- [7] COMSOL. Laminar flow Module User’s Guide, version 5.5. Technical report, 2020.
- [8] COMSOL. Transport of diluted species Module User’s Guide, version 5.5. Technical report, 2020.
- [9] Anis Younes, Marwan Fahs and Selim Ahmed. Solving density driven flow problems with efficient spatial discretizations and higher-order time integration methods. *Advances in water resources*, 32(3):340–352, 2009.
- [10] Xiaonan Shi, Tingwu Lei, Yan Yan and Fan Zhang. Determination and impact factor analysis of hydrodynamic dispersion coefficient within a gravel layer using an electrolyte tracer method. *International Soil and Water Conservation Research*, 4(2):87–92, 2016.
- [11] Fidel Toldrá. *Dry-cured meat products*. John Wiley & Sons, 2008.
- [12] Hiroyuki Kitahata and Natsuhiko Yoshinaga. Effective diffusion coefficient including the marangoni effect. *The Journal of chemical physics*, 148(13):134906, 2018.
- [13] K.G. Nayar, D. Panchanathan, G.H. McKinley and J.H. Lienhard. Surface tension of seawater. *Journal of Physical and Chemical Reference Data*, 43(4):043103, 2014.
- [14] Mostafa H. Sharqawy, John H. Lienhard and Syed M. Zubair. Thermophysical properties of seawater: a review of existing correlations and data. *Desalination and water treatment*, 16(1-3):354–380, 2010.
- [15] Matthew O Reese, Suren A Gevorgyan, Mikkel Jørgensen, Eva Bundgaard, Sarah R Kurtz, David S Ginley, Dana C Olson, Matthew T Lloyd, Pasquale Morvillo, Eugene A Katz, et al. Consensus stability testing protocols for organic photovoltaic materials and devices. *Solar Energy Materials and Solar Cells*, 95(5):1253–1267, 2011.
- [16] Yanbin Yun, Runyu Ma, Wenzhen Zhang, AG Fane, and Jiding Li. Direct contact membrane distillation mechanism for high concentration nacl solutions. *Desalination*, 188(1-3):251–262, 2006.